International Journal of Marine Energy 20 (2017) 1–16

Contents lists available at ScienceDirect

International Journal of Marine Energy

journal homepage: www.elsevier.com/locate/ijome

Tidal energy resource characterization in Chacao Channel, Chile

Maricarmen Guerra [a,*], Rodrigo Cienfuegos [b,c,d], Jim Thomson [a], Leandro Suarez [c]

[a] Applied Physics Laboratory, University of Washington, Seattle, WA, United States
[b] Departamento de Ingenieria Hidraulica y Ambiental, Pontificia Universidad Catolica de Chile, Santiago, Chile
[c] MERIC - Marine Energy Research and Innovation Center, Santiago, Chile
[d] Centro Nacional de Investigación para la Gestión Integrada de Desastres Naturales (CIGIDEN), Santiago, Chile

ARTICLE INFO

Article history:
Received 31 May 2017
Revised 30 September 2017
Accepted 9 November 2017
Available online 11 November 2017

Keywords:
Tidal energy
Tidal currents
Turbulence
Chacao Channel

ABSTRACT

Chacao Channel is an energetic tidal channel located at the northernmost part of the Chilean Patagonia. The channel has been previously identified as a prospective site for tidal energy extraction, however there has been only a limited understanding of the tidal flows. A new set of field measurements distributed along Chacao Channel is presented here for tidal energy resource characterization, including tidal elevations, tidal currents (in space and time), and turbulence. The field data also are used to calibrate and validate a FVCOM hydrodynamic numerical model of the entire channel, which is then used for tidal energy resource assessment. Field measurements indicate that tidal elevation range increases eastward along the channel, that tidal currents exceed 4 ms^{-1} at some points within the channel, and that turbulence intensity ranges between 5 and 20%. The data and numerical model results are used to estimate the kinetic power density of the tidal currents at Chacao Channel, which is in average 5 kWm^{-2}.

1. Introduction

Historically, electricity in Chile has been mainly generated from hydroelectric dams (nearly 80% in the 1980s) [1]. In recent years, hydroelectricity generation has reduced to 43% on average from 2010 to 2014. The variability of hydrological conditions has prompted the search for reliable forms of electricity generation, and thus electricity at present is mostly generated from fossil fuels (52%, natural gas and coal) [1,2]. Due to this shift in the Chilean energy matrix, the Chilean government has set as goal to produce 60% of its electricity from renewables by 2035, and 70% by 2050 [1] (Note that these renewable percentages include hydroelectricity). In this context, tidal energy is an enticing source of renewable energy for Chile, as the chilean coast has been recognized to be one of the most energetic in South America [3]. Among the priority sites along the Chilean coast, Chacao Channel (S 41°; W 74°) has been previously recognized as the most suitable site for tidal energy extraction considering its available resource and its proximity to the electrical grid [3]. However, the resource assessment is based on a global model prediction using coarse bathymetry. A detailed resource characterization is then necessary for selecting promising areas for tidal energy extraction within the channel, for better power extraction estimations, and for appropriate turbine design [4,5].

According to guidelines from the European Marine Energy Center (EMEC), the tidal energy resource characterization at a specific tidal channel should include long-term measurements of tidal currents (from which tidal harmonics can be

* Corresponding author.
E-mail addresses: mguerrap@uw.edu (M. Guerra), racienfu@ing.puc.cl (R. Cienfuegos), jthomson@apl.washington.edu (J. Thomson), leandro.suarez@meric.cl (L. Suarez).

https://doi.org/10.1016/j.ijome.2017.11.002
2214-1669/

calculated) together with hydrodynamic numerical models that expand the information from the field measurements [6]. Field measurements typically use Acoustic Doppler Current Profilers (ADCPs), which provide time series of the three velocity components at different depths in the water column. Up-looking bottom-mounted ADCPs are used to analyze the temporal variability in the tidal currents at a single location [5,7–9], while down-looking ship-mounted ADCPs are used to analyze tidal current variation in space [10,8].

A wide range of different hydrodynamic numerical models are used to characterize the tidal energy resource [11,12]. Simple analytic models, such as Garrett and Cummins (2008) [13], are also used in resource assessment. Three-dimensional (3-D) models are currently the choice for tidal energy resource assessment [11], since they provide information about the vertical structure of velocity, and hence a better estimation of available power. In Lewis et al. (2015) [4], ROMS (Regional Ocean Modeling System) is used to evaluate the tidal energy resource in the Irish Sea; a sensitivity analysis on grid resolution indicates that a resolution of less than 500 m is required for a regional-scale resource assessment [4]. Tang et al. (2014) [12] evaluated the tidal energy potential along the New Jersey coast using the unstructured FVCOM model, with resolutions as fine as 10 m, and this allowed for a detailed representation of the New Jersey coastline. The most favorable sites were found in the mouths of bays, narrow channels, and headlands [12].

In addition to mean flow conditions (needed for power estimations), time and space characterization of ambient turbulence is also necessary for tidal energy resource characterization. At a single location in space, the total tidal current velocity $\mathbf{u}(z)$ can be decomposed as:

$$\mathbf{u}(z) = \overline{\mathbf{u}} + \tilde{u} + u' \tag{1}$$

where $\overline{\mathbf{u}}$ represents the deterministic currents, including both harmonic and anharmonic components. The deterministic currents are usually dominated by harmonic constituents associated with lunar and solar forcing, while anharmonic currents result from interaction with the local bathymetry [14,5]. Wave and wind induced currents, and residual flows, are represented by $\tilde{u}$, and these are not the focus of this study. Finally, u' refers to the turbulent fluctuations of the mean current, spanning from large-scale two-dimensional eddies to small-scale isotropic eddies [14].

Turbulence has a significant impact on turbine performance and durability [15–17], as well as extension and recovery of the wake behind the turbine [18]. Many turbulence parameters can be estimated from ADCP measurements, if variance due to noise is correctly removed from the raw data. However, Acoustic Doppler Velocimeters are the preferred instrument for turbulence measurements, as they record velocities at high-sampling frequencies with low noise, and thereby allow fto resolve a wide range of turbulence scales. Osalusi et al. (2009) [19] characterize the turbulent structure, and turbulence evolution, at EMEC's tidal energy site using ADCPs measurements. Osalusi et al. (2009) [19] estimate Reynold's stresses, and Turbulent Kinetic Energy (TKE) production and dissipation rates. Thomson et al. (2012) [14] examine the ambient turbulence at two prospective tidal energy sites in Puget Sound, WA., using both ADCPs and ADVs. A set of turbulence statistics and turbulence estimation techniques are provided, which are useful to estimate turbine design loads [14]. The studied turbulence parameters include, among others, noise-corrected turbulence intensity, TKE frequency spectra, and the examination of an approximate TKE balance. However, the authors emphasize that turbulence measurements from ADCPs are limited by their higher Doppler noise (which needs to be removed), and by the bin sizes (which limit the observed turbulence length scales) [14].

1.1. Site description

Chacao Channel is an energetic tidal channel located in the north of the Chilean Patagonia fjord region (S 41°; W 74°). The channel separates mainland Chile (to the north) and Chiloé Island (to the south). In the east–west direction, it connects the Chilean Inland Sea (CIS) to the Pacific Ocean, via the Gulf of Ancud. The channel is approximately 40 km long and about 2.5 km wide in its narrowest part. The map on Fig. 1 shows the location of Chacao Channel within the Chilean Inland Sea region. The flow in Chacao Channel exhibits a periodic behavior dominated by astronomic tides with the M_2 semi-diurnal component being the most significant one [20]. Previous investigations report the presence of high tidal amplitudes and currents, up to 6 m and 4 ms^{-1}, respectively, during spring tides [20,21]. The circulation in Chacao Channel is weakly influenced by river discharge, with typical salinities around 30 [20].

Chacao Channel is the entrance to the Chilean Patagonia, an area characterized by pristine landscapes and fjord-like channels. This area is expected to receive high pressure from infrastructure and energy projects in the future [22]. Chacao Channel is regionally important for environmental, social and economic reasons. The channel is home to a great diversity of benthic organisms and mammals. It is, for example, one of the few sites where a blue whale has been sighted [23,24]. Chacao Channel has eight fishing villages, where more than 4,000 artisan fishermen work and more than 25,000 tons of fisheries resources are extracted every year [25]. Despite its importance to the Chilean society, the knowledge of Chacao Channel's hydrodynamics is limited. The previous published hydrodynamic investigations focused on Chacao Channel are the works of Cáceres et al. (2003) [20] and Aiken (2008) [21]. Both emphasized the energetic behavior of the channel and its complex hydrodynamics.

Caceres et al. (2003) [20] studied the across channel flow structure at the narrowest part, where a large pinnacle, known as Roca Remolinos, exists in the center of the cross section. They analyze the across channel velocity variations as the strong tidal flows interact with the pinnacle, and they present estimates for the terms of the across channel momentum balance

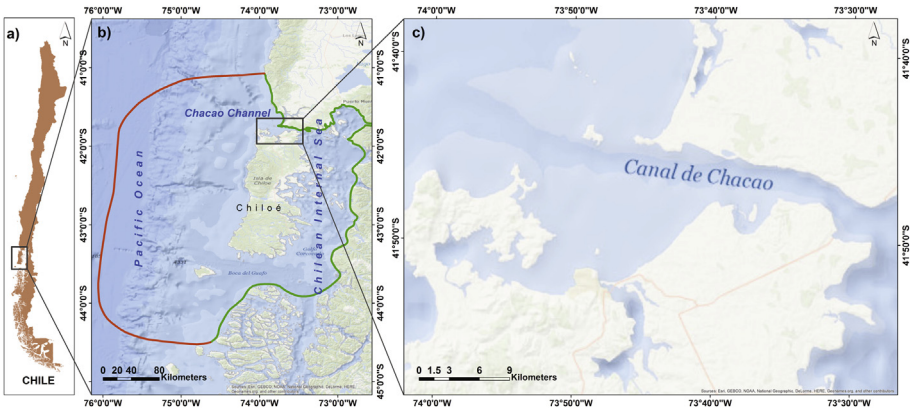

Fig. 1. a) Chacao Channel location in the south of Chile, b) Northern portion of Chilean Internal Sea, FVCOM domain boundaries in green, and FVCOM forcing boundary in orange, and c) Chacao Channel.

equation. The main findings suggest nonlinear interactions between the flow and the bathymetry, which cause a strong lateral structure of residual flows, wherein there is an outflow in the deep channels and inflows on the shoals [20]. Aiken (2008) [21] studied the propagation of tidal waves from the Pacific Ocean into the Chilean Inland Sea (CIS) region (shown in Fig. 1), with a focus on the behavior of tidal constituents within the CIS. Numerical investigations of barotropic tides are conducted using a ROMS model of the entire CIS [21]. Aiken showed tidal amplification within the northern part of the CIS (located southeast of Chacao Channel) due to the resonance of tidal waves as they interact with the basin geometry. This resonance is thought to be responsible for the large range of tidal elevations at the east end of Chacao Channel, which in turn drives the strong tidal currents [21].

In the present study, conventional methods for tidal energy resource characterization and assessment are applied to Chacao Channel. The field characterization, described in Section 2.1, includes sea-level measurements from tidal gauges, tidal current measurements from fixed and shipboard ADCPs at multiple locations, and a detailed characterization of turbulence using moored ADVs at a single location [26]. An FVCOM model [27] was prepared for the Chacao Channel region, using the field data for calibration and validation of the model (Section 2.2). The data analysis includes harmonic analysis of tidal elevation and tidal currents, quantification of spatial gradients in tidal currents, spectral analysis of turbulence, and the estimation of available power density (Section 3). The hydrodynamics of Chacao Channel are briefly analyzed in a discussion section.

2. Methods

2.1. Field measurements

The Chacao Channel field campaign consisted of multi-month sea level and tidal current measurements at several fixed locations throughout the channel, along with short-term measurements of spatial gradients and turbulence in a single area.

The locations of the instruments are shown in Fig. 2, where stars represent tidal gauges distributed along the south and north banks of the channel, and circles show the position of the acoustic Doppler instruments used for tidal current measurements. Previous bathymetric information of the channel is available through nautical charts from the Chilean Navy, but these are too coarse to be used in a detailed numerical model of the channel. New multi-beam bathymetry is available for this investigation. The new 10 m resolution channel bathymetry is shown in Fig. 2. From west to east a deeper longitudinal channel is observed, beginning offshore of Carelmapu fishing village. At the narrowest part, the Roca Remolinos is observed, and it is surrounded by the deeper portion of the channel ($\sim$ 200 m) (This feature is the focus of Caceres et al. (2003) [20]). The channel ends in a deep semi-enclosed bay known as Gulf of Ancud.

2.1.1. Tidal elevation

Five tidal gauges were distributed along the south and northern banks of Chacao Channel to quantify time and space variations of the sea level. The specific location of each tidal gauge is shown in Fig. 2. The tidal gauges collected data for over 30 days between May and June 2012. The gauges were set up to register sea level variations every 5 min with a 10 m range. The data were referenced to a unique horizontal plane, defined by the mean sea level at the Carelmapu station.

2.1.2. Tidal currents

2.1.2.1. Deterministic velocities. Similarly to the sea level measurements, deterministic tidal currents in Chacao Channel were measured by six bottom-mounted RDI Workhorse Sentinel Acoustic Doppler Current Profilers (ADCPs) distributed along the

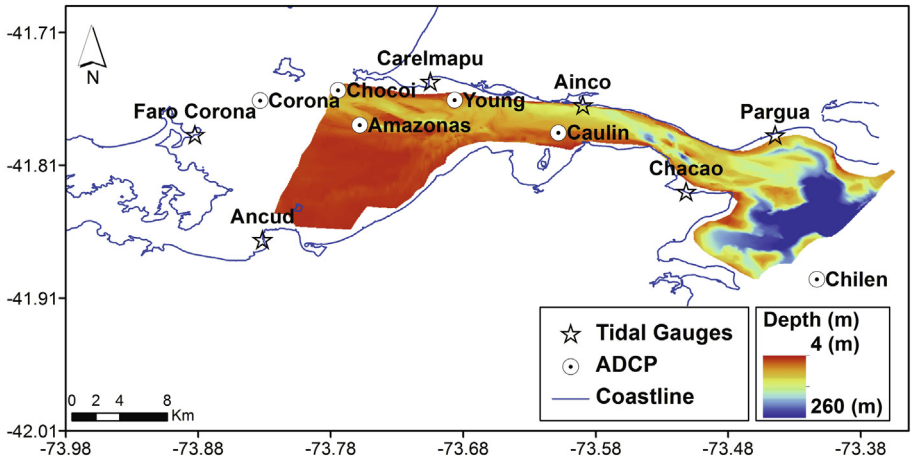

Fig. 2. Chacao Channel high-resolution multi-beam bathymetry and instruments location along the channel. Stars represent the location of tidal gauges used to measure tidal elevation, and circles represent the location of the ADCPs used for the multi-month characterization of tidal currents.

channel between May and July 2012. The maximum depth of installation was approximately 40 m due to logistical constraints in the deployments. Each Doppler profiler measured three components of velocity at 1 Hz sampling frequency, then averaged these measurements every 10 min. These measurements were in vertical profiles, in bins spaced every 2 m.

To characterize the local spatial variability of tidal currents a set of measurements was conducted following the station-keeping procedure described in [10]. Station-keeping is a vessel-based methodology originally developed to map small-scale variations of tidal currents as gradients between select stations. Using a vessel-mounted ADCP, vessel position is maintained at each target station for a short period of time and then each station is reoccupied several times during the same tidal cycle. At Chacao Channel, measurements were collected at the corners and center of a 500 m square centered at the Young site (S 41°45.746′; W 73°40.949′) on February 12, 2013 (see Fig. 7 for station-keeping locations). Each of the five stations were surveyed five times during one ebb and four times during one flood tide. The measurements at each station were not simultaneous, but they were conducted during the same ebb tide and during the same flood tide for all stations. The ADCP was an RDI Workhorse 1200 kHz ADCP pole-mounted to the R/V Dr. Jurgen Winter. The ADCP was set to measure three components of velocity at 2 Hz in bins spaced every 3 m, down to 30 m depth. The ADCP transducer was located 1.25 m bellow water level, and there was a 2 m blanking distance.

2.1.2.2. Turbulent velocities. Turbulent velocity fluctuations were measured in a short-term deployment at the Young site, which was chosen due to its high and consistent currents, as previously detected during the long-term (deterministic) ADCP measurements. Turbulence measurements were taken using Acoustic Doppler Velocimeters (ADVs), since they are more precise than ADCPs. Specifically, ADVs provide high frequency velocity measurements with much lower Doppler noise. The ADVs were deployed on the Tidal Turbulence Mooring (TTM), in which the instruments are in-line along a tension mooring [26,28,29]. The TTM deployed in Chacao Channel consisted of a heavy anchor (approx. 1000 kg weight) to hold the mooring in place, a buoy (approx. 300 kg buoyancy), to hold the mooring vertical, and an instrument vane inline between anchor and buoy. Two 6 MHz Nortek Vector ADVs were mounted on the instrument vane. The instruments are referred to according to the institutions providing them (i.e., the NREL ADV and the APL ADV). The two instruments targeted a tidal turbine's nominal hub-height (10 m from the sea-bottom). Both ADVs were oriented to point into the flow under all conditions (i.e., flood and ebb) by using swivels above and below the vane. The ADVs sampled the tidal currents at 16 Hz in their local XYZ coordinate system. The nominal velocity range was set at 2 ms^{-1} (along-beam), which gives approximately 3.5 ms^{-1} horizontal range.

The TTM deployment lasted 2.5 days, between 11 and 14 February 2013; this was a short deployment since the long-term characterization of tidal currents was already conducted via the multi-month deployment. The deployment site is approximately 38 m deep (relative to mean lower low water) and was approximately the same position as the Young ADCP deployment.

Contamination from mooring motion needs to be removed from turbulent velocities prior to the data analysis. For this deployment inertial motion units (IMU) were attached to each ADV in order to sample mooring acceleration (both linear and rotational) and orientation. The NREL ADV had a Microstrain 3DM-GX3 motion sensor with synchronous data acquisition; the APL ADV had a x-IMU motion sensors with asynchronous data within 1 s of the velocity data [26]. Direct motion correction [26,29], which requires synchronous data acquisition between raw velocities and mooring acceleration and rotation, was applied to every point of the time series of the NREL ADV measurements. For the asynchronous motion data ADV, only a correction based on burst-averaged mooring orientation angle was applied. For this deployment, turbulent kinetic energy spectral density comparisons between the two corrected data sets show that differences are not significant when the full motion correction was not applied (shown bellow in Fig. 9c)). This is because the site is highly energetic, and the

turbulence signals are much larger than the motion contamination signals. The variance of the turbulence signal is of $\mathcal{O}(10^0)$ m^2s^{-2}, while the variance of the motion contamination signals is of $\mathcal{O}(10^{-1})$ m^2s^{-2}.

2.2. Hydrodynamic numerical model

A numerical model of Chacao Channel was constructed to extrapolate the field measurements. This allows a study of the large spatial variations of the tidal flows in Chacao Channel, as thereby assessment of the tidal resource at potential sites throughout the Channel. The Finite-Volume Community Ocean Model (FVCOM; [27]) is used for this purpose. FVCOM is a three-dimensional, non-structured, finite-volume hydrodynamic model that solves the primitive ocean circulation equations [27]. FVCOM is widely used in the study of physical and biological processes in coastal regions characterized by complex bathymetry and diverse forcing (tides, wind, river discharge, etc.). For a detailed description of FVCOM model, the reader is referred to [27] and to the FVCOM user manual [30].

The hydrodynamic model covers the portion of Chilean Sea surrounding the island of Chiloé, including the Chacao Channel and part of the continental shelf. This domain size is necessary to: i) assess the propagation of tidal waves in the south of Chiloé Island; ii) observe the resonance phenomenon in the Chilean Internal Sea (east of Chiloé) previously described in [21]; and iii) to fully develop the flow that will enter Chacao Channel through the east end.

The study domain extends approximately 66,400 km^2. It is discretized in a non-structured mesh of approximately 50,000 triangular elements with a resolution ranging from 5000 m, in the open ocean, up to 50 m in Chacao Channel. The model bathymetry is constructed from the new high resolution bathymetric measurements within Chacao Channel, together with nautical charts from the Hydrographic and Oceanographic Service of the Chilean Navy (SHOA) for areas where no new surveys were made. Although the SHOA information is coarse, it is the only bathymetry available for the area. The one external forcing applied in the simulations were tides. The model was forced from its western edge using 34 astronomical tidal harmonic components obtained from the global model TPXO 7.1 [31]. The simulation domain is shown in Fig. 1. The model limits are denoted by a green line, while the orange line denotes the forcing boundary.

The hydrodynamic model was run from May 4th 2012 until July 7th 2012 (considering 3 days to spin-up the model). This date range includes the long-term tidal elevation and tidal current measurements, and it is sufficient to map the main harmonic components of the tidal flow of Chacao Channel. The time step was 0.2 s, and the output was saved every 30 min. The default turbulent closure schemes were used for the estimation of the vertical eddy viscosity and horizontal diffusion coefficients, namely the modified Mellor and Yamada level 2.5 [32] and Smagorinsky [33] models.

3. Analysis

3.1. Tidal elevation

Tidal elevation at Chacao Channel varies in time and space. In time, the tidal elevation is characterized by a semidiurnal harmonic behavior at all stations, featuring two low and two high tides each day of slightly different magnitude. Fig. 3 shows two tidal elevation time series from Carelmapu and Pargua tidal gauges. The measurement period covered more than one lunar cycle, capturing at least two neap and two spring tides at each station. Spatial variations of tidal elevation show a considerable increase in range from west to east. The maximum observed tidal elevation range at Carelmapu (west) tidal gauge is 3.7 m, while at Pargua (east) the maximum range is 6.9 m. The diurnal inequality was also observed to increase from west to east within Chacao Channel, specially during spring tides. For the spring tide observed around day 17 (Fig. 3) the high tide inequality at Carelmapu was 0.69 m, while the high tide inequality at Pargua was 0.96 m. For the same spring tide, there was an approximate 40 min lag between the occurrence of higher-high tide between Carelmapu and Pargua.

Harmonic analysis of tidal elevation has been conducted using the *t_tide* software developed by [34]. The analysis indicates that the most energetic component at Chacao Channel is the principal lunar semidiurnal M_2 component. Results for the M_2 tidal component are shown in Table 1. The following four most energetic components are the semi-diurnal S_2 and N_2, and

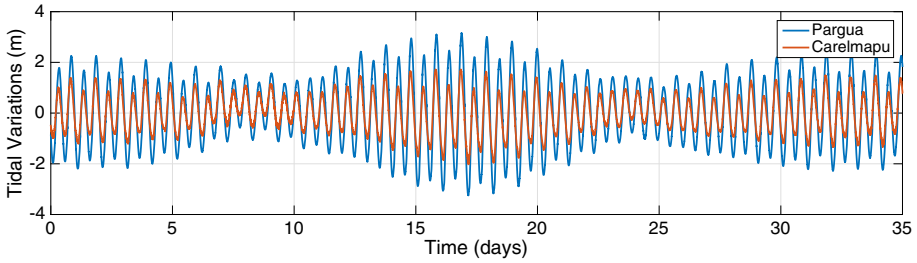

Fig. 3. Tidal elevation variations at Carelmapu (red) and Pargua (blue) tidal gauge stations relative to their respective mean sea level elevation.

Table 1
M_2 tidal component characteristics for tidal elevation and for 10 m above the sea-bottom tidal currents at tidal gauges and ADCP stations, respectivelly.

Tidal Amplitude						
Tidal Gauge	Corona	Ancud	Carelmapu	Ainco	Chacao	Pargua
Amplitude (m)	0.61	0.66	0.92	1.25	1.63	1.75
Phase (°)	122.91	124.60	140.77	140.68	130.55	153.28
Tidal Ellipse						
ADCP Station	Corona	Chocoi	Amazonas	Young	Caulin	Chilen
Semi-major axis (m/s)	1.57	2.01	1.83	1.91	1.80	0.33
Semi-minor axis (m/s)	0.13	0.31	0.07	0.01	0.03	0.01
Phase (°)	227.25	184.23	205.80	186.82	204.65	193.16
Inclination (°)	2.88	2.58	3.05	3.12	3.13	2.56

the diurnal lunar O_1 and K_1 components. The M_2 amplitude is about 0.6 m on the west mouth of the channel, increasing to 1.75 m at Pargua station. According to [21], the M_2 tidal elevation amplitude is expected to continue to increase within Gulf of Ancud and north to Reloncaví Sound.

3.2. Tidal currents

3.2.1. Deterministic currents

The following analysis is focused in the horizontal velocity components, and the horizontal velocity magnitude and direction at each depth of the water column. The horizontal velocities are the relevant resource for extraction by tidal turbines, and, furthermore, the observed vertical velocities are two orders of magnitude smaller than horizontal velocities. The horizontal current magnitude is defined as $U = \sqrt{u^2 + v^2}$, where u and v represent the east and north velocities respectively. As general convention, a negative U indicates ebb current (seaward) and a positive one, flood current (landward).

Tidal currents at Chacao Channel present a semidiurnal regime, with two ebb and two flood currents of different magnitude each lunar day. Harmonic analysis of tidal currents is performed using the widely used *t_tide* software from [34]. The M_2 tidal current component is predominant at all ADCP stations, being one order of magnitude greater than the next most energetic components. Results for the M_2 tidal component are shown in Table 1. M_2 tidal ellipses for horizontal current at 10 m above the sea-bottom for all ADCP stations are shown in Fig. 4. M_2 ellipse orientation and axis magnitudes vary along the channel. From west to east, ellipse orientation aligns with the channel's main axis. Semi-major axis values of M_2 current remain fairly constant along the channel (contrary to tidal elevation magnitude), then greatly decrease at Chilen station, which is outside the channel's boundaries. At Corona ADCP station the M_2 semi-major amplitude is 1.6 ms^{-1}, and approximately 2 ms^{-1} at Chocoi, Amazonas, Young and Caulin stations. Semi-minor axis M_2 values decrease as the flow gets constrained into the channel, resulting in small cross-channel flows (and large along-channel flows).

Polagye & Thomson (2013) [5] provides a series of metrics based in velocity time-series that are useful for tidal energy resource characterization, and a set of Matlab functions to perform the analysis of velocity data is available on the Northwest National Marine Renewable Energy Ceneter website [5]. The following analysis of bottom-mounted ADCP data is performed using those Matlab functions.

Fig. 5 shows a record of the horizontal current magnitude together with flow direction along the water column at the Young station. Harmonic behavior of horizontal currents is observed through the water column; spring and neap tidal currents are clearly observed. The maximum horizontal current observed at this site was approximately 3.5ms^{-1} at ebb tide. As seen in the record, direction varies from $\sim 90^\circ$ (ebb) to $\sim -90^\circ$ (flood), which is consistent with the channel's geometry and orientation.

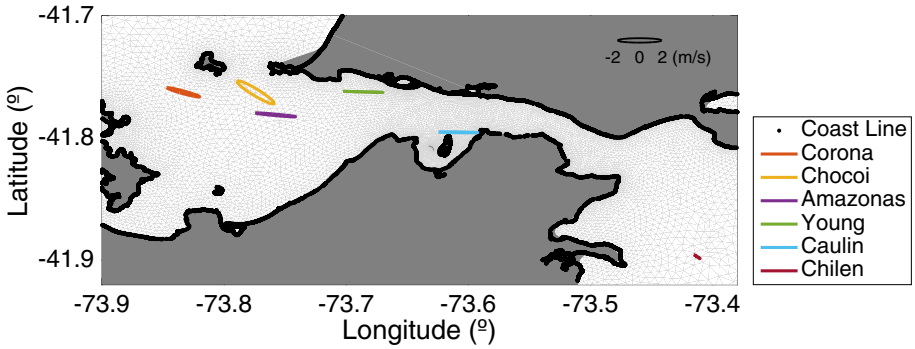

Fig. 4. M_2 tidal ellipses at 10 m above the sea-bottom at each ADCP station along Chacao Channel.

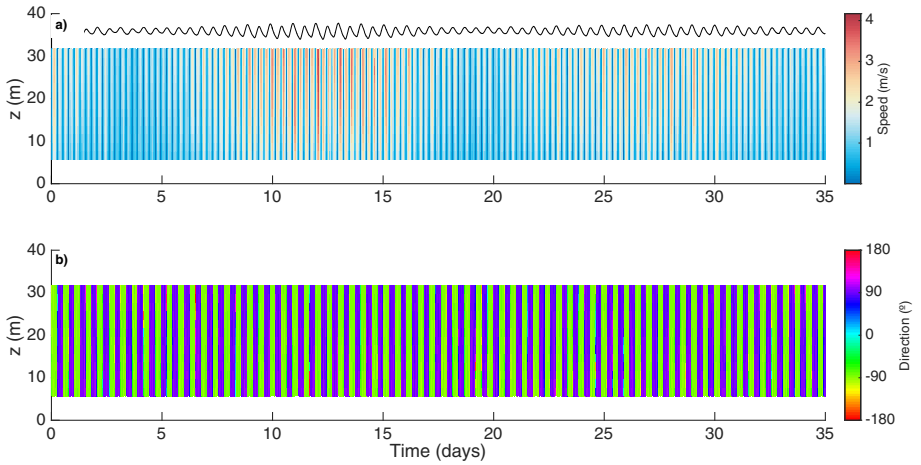

Fig. 5. a) Horizontal speed , and b) flow direction, recorded at Young station in 2012. Analysis performed with methodology from [5].

Fig. 6 shows vertical profiles of time-averaged horizontal velocity during the measurement period, separated by ebb and flood tides. The plots show enhanced ebb currents at all depths for all stations. At Young, the ebb/flood asymmetry indicates that mean ebb current is about 10% greater than flood mean current at all depths. However, this ebb/flood magnitude asymmetry is not significant at all stations. For example, at Caulin, ebb/flood asymmetry is less than 1%. Regarding direction, the flow within Chacao Channel is mainly constrained by its west-east orientation. At Young, the principal direction of the flow is close to 90° from North, and there is small ebb/flood directional asymmetry (maximum 4°). The direction is more variable along the water column during the flood currents.

Results from the station keeping procedure around Young station are shown in Fig. 7. The station-keeping data was collected and processed according to the methodology presented in [10]. Results shown in Fig. 7 b) and c) correspond to bin 3 of

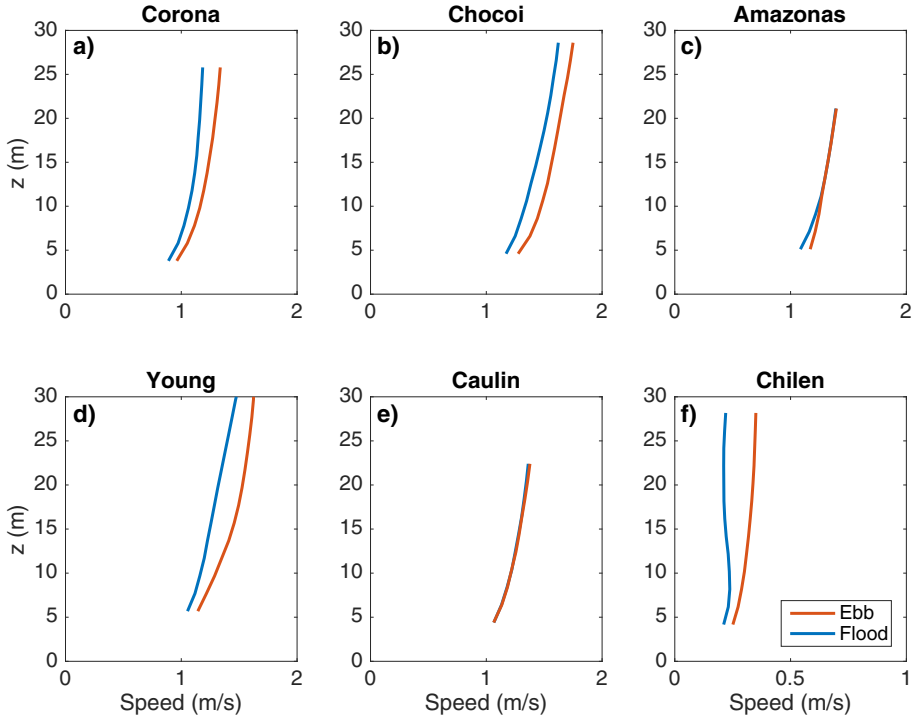

Fig. 6. Vertical profiles of time-averaged horizontal speed at ADCP stations separated by ebb and flood: a) Corona, b) Chocoi, c) Amazonas, d) Young, e) Caulin, and f) Chilen. Ebb tide is in red, flood tide is in blue. Note the different scale in the Chilen station plot, this ADCP was located outside of the main Chacao Channel area. Profiles are estimated using the methodology from [5].

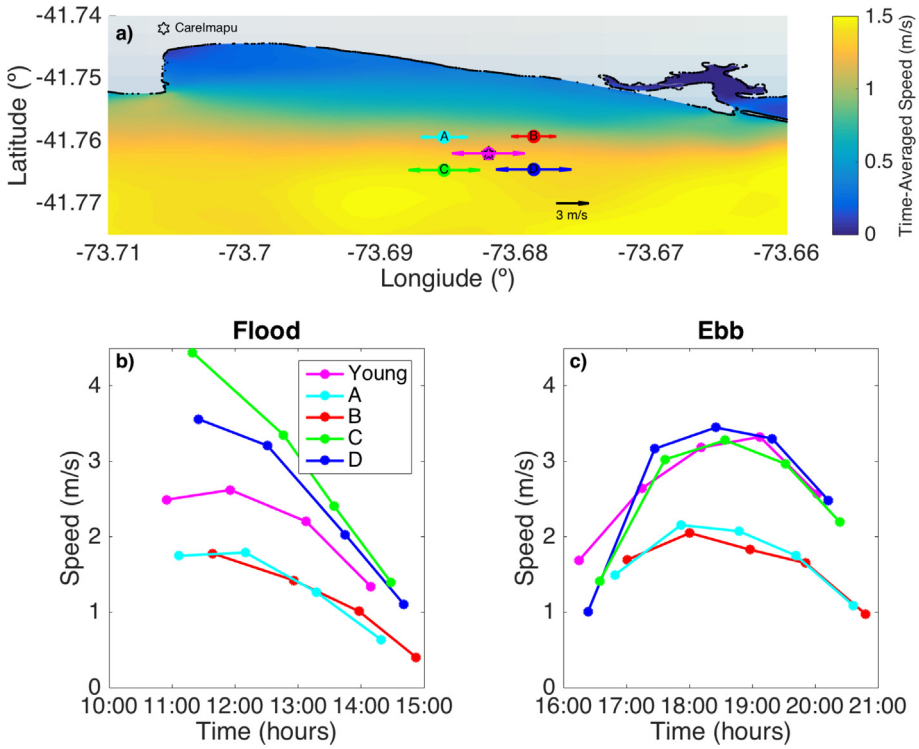

Fig. 7. Station-keeping velocities around Young station: a) Station-keeping measurement locations, maximum recorded ebb and flood velocity magnitude (arrows) at each of the station-keeping target locations, and colormap of time-averaged speed from FVCOM model, b) Time-series of flood tide station-keeping results, and c) Time-series of ebb tide station-keeping results. Legend in b) and c) correspond with station-keeping locations from a).

the down-looking ADCP, located 10.75 m bellow the free surface. At all stations, bin 3 was located in the free-stream portion of the velocity vertical profile, well outside the bottom-boundary layer.

High local variability in currents is observed in the across-channel direction and between ebb and flood tide. Stations closer to the shore, A and B, show significantly smaller currents than offshore stations C and D, which are only 500 m apart. During ebb tide, the currents increase from 2 ms^{-1} to 3.5 ms^{-1} in the across-channel direction, resulting in a mean gradient of 0.3 ms^{-1} every 100 m. Spatial variability is enhanced during flood tides where maximum current increases from about 2 ms^{-1} on stations A and B, to more than 4 ms^{-1} at stations C and D. Also during flood tide, a large longitudinal variability is observed between stations C and D. These differences might be explained by the shallower and slower flow area generated by the headland located east of Carelmapu. This slower flow area is observed in the numerical model results, which are shown as a colormap in Fig. 7a). Note that stations A and B are just in the edge of this area.

These results illustrate the complex flow field variations in Chacao Channel. These large spatial gradients in velocity are of great importance for tidal energy resource assessment and the distribution of tidal turbines, as a variation of 0.3 ms^{-1} in currents is equivalent to approximately a 1.4 kWm^{-2} variation in power density.

3.2.2. Turbulent velocities

Turbulent variations of the mean flow are characterized in terms of turbulent intensity and turbulent kinetic energy spectra. Velocity data obtained from the ADVs onboard the TTM were corrected for TTM motions, quality-controlled to remove points with low acoustic correlations, and despiked using a 3D phase space method of Goring and Nikora (2002) [35]. Velocity data were processed in five minute bursts in order to ensure flow stationarity in the turbulence time-series and to capture the large scale turbulence (i.e., short enough to have a stable mean current, yet long enough to have reliable statistics) [14,36].

For every five minute burst of ADV data, the noise corrected turbulence intensity (TI) [14] is defined as:

$$TI = \frac{\sigma_u}{\overline{u}} = \frac{\sqrt{\sigma_u^2 - \sigma_n^2}}{\overline{u}} \tag{2}$$

where σ_u^2 is the variance of the velocity fluctuations, σ_n^2 is the instrument Doppler noise variance, and $\overline{u}$ is the mean along-channel velocity. The instrument's Doppler noise variance provided by the manufacturer is equal to 2×10^{-4} m^2s^{-2}. Mean along-channel flow velocity and turbulent intensities are shown in Fig. 8. As expected, the along-channel velocity shows an

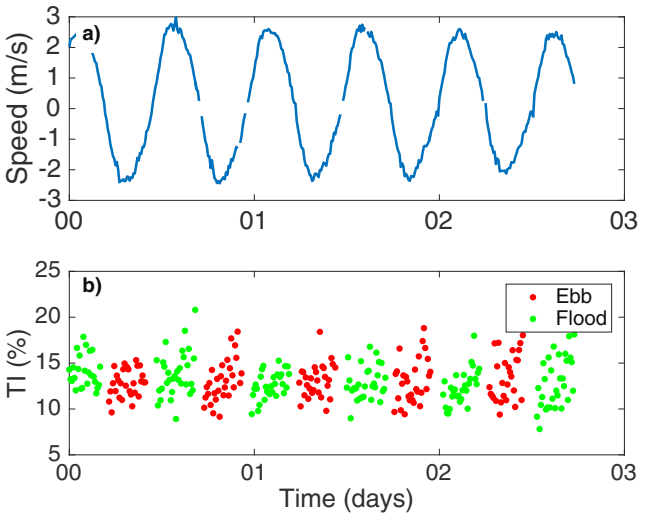

Fig. 8. a) Mean along-channel velocity (5-min time-averages), and b) turbulence intensities estimated from the February 2013 turbulence measurements at Young station.

harmonic behavior. TI ranges from 5 to 20% at the site, similar to other energetic tidal channels such as Admiralty Inlet, WA. [14], however the turbulent intensity does not seem to follow a clear trend with the mean flow during the deployment.

The distribution of turbulent kinetic energy among eddies of different sizes is represented trough the turbulent kinetic energy spectra. Frequency spectra of horizontal along-channel velocities and vertical velocities are calculated for every five minute burst using six 75 s sub-windows with 50% overlap and a Hanning data taper, which results in a spectral density estimate with 16 degrees of freedom. Each spectra, $S(f)$, corresponds to the turbulent kinetic energy (TKE) components of velocity such that $\overline{u'^2} = \int S_u(f)df$ and $\overline{w'^2} = \int S_w(f)df$.

All 5-min spectral density estimates are bin-averaged by mean along-channel velocity (0.5 ms^{-1} bins) for clarity of the presentation. These bin-averaged spectra are shown in Fig. 9. All spectra are well sorted by mean flow velocity, indicating that total TKE increases as mean velocity increases. Three regions are distinguished on the TKE spectra for both along-channel and vertical velocity components. At low frequencies ($f < 0.2$ Hz), a region of anisotropic turbulence is observed, in which TKE reaches a maximum and remains fairly constant as frequency decreases, probably limited by the channel's lateral length scales. TKE from vertical motions is one order of magnitude smaller than TKE from horizontal motions at low frequencies (Fig. 9(c)), consistent with the presence of anisotropic turbulence and limitation of vertical motion by the depth of the channel. At mid frequencies ($0.2 < f < 2$ Hz), an isotropic region of three-dimensional turbulence is present, which follows the classic $f^{-5/3}$ Kolmogorov's inertial subrange slope [37]. In this region TKE is transferred from large scale eddies to short scale eddies until energy is dissipated by viscosity at even smaller scales. At higher ($f > 2$ Hz) frequencies, the spectrum becomes affected by the inherent Doppler noise of the instrument [38]. A white-noise energy level is observed around $S(f) = 10^{-4}$ m^2s^{-2} Hz^{-1}.

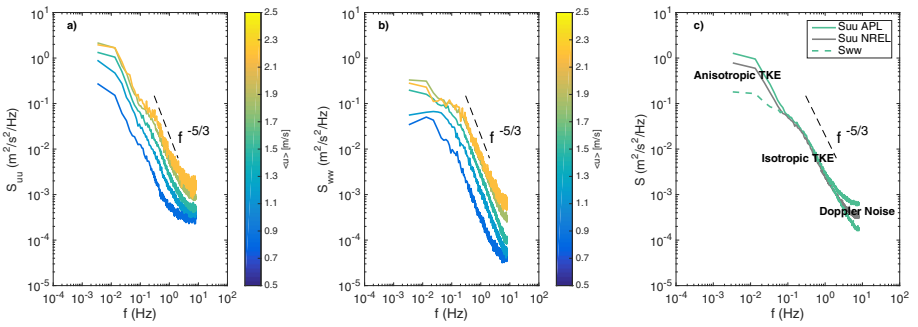

Fig. 9. Turbulent kinetic energy spectral density estimates from APL ADV data bin-averaged by mean flow velocity: a) along-channel TKE spectra sorted by mean flow velocity conditions, b) Vertical TKE spectra sorted by mean flow velocity conditions, and c) along-channel and vertical TKE spectra averaged across all mean flow velocity conditions, averaged along-channel TKE spectra from NREL ADV is included in gray. Dashed black lines show the theoretical $f^{-5/3}$ energy cascade.

3.3. Hydrodynamic numerical model

The FVCOM numerical model results are validated by comparisons of tidal elevations, tidal currents, and turbulence parameters. The model results agree well with field measurements in terms of tidal elevation and tidal currents.

Tidal elevation harmonic components are well represented by the numerical model. Estimated amplitude of the M_2 tidal elevation component falls within the 95% confidence intervals for all tidal gauges stations. The relative differences of component amplitudes are less than 10%, however phase differences vary between 40° and 60° for the M_2 component at the tidal gauges stations.

Fig. 10a) shows the M_2 tidal elevation component along the CIS, and Fig. 10b) shows this component within Chacao Channel. The tidal elevation amplification and phase change are well-captured by the FVCOM model, which is forced using 34 tidal components at the same time and includes the detailed bathymetry in Chacao Channel. The M_2 tidal elevation amplitude increases by a factor of 4 from the CIS south entrance (south of Chiloé Island) towards the Ancud Gulf (Chacao Channel east end), while the phase changes 23° (not shown). This tidal wave amplification results approximately in a 2 m M_2 amplitude difference between the ends of Chacao Channel, consistent with both the tidal gauge observations and the Aiken (2008) [21] results.

Tidal ellipses of depth integrated velocities are compared for evaluating model performance in reproducing tidal currents. The model correctly represents the semi-major and semi-minor tidal ellipses axes, and the inclination of the ellipses at all stations. The main model-data differences are again in tidal phase, which vary between 4° and 18° for the M_2 tidal current component. Vertical profiles of time-averaged horizontal speeds (averaged over the FVCOM simulation period) at the different ADCP stations are estimated following the tidal energy resource characterization methodology from [5]. FVCOM time-averaged vertical profiles of horizontal speeds agree well with the data at the ADCP stations located within Chacao Channel; relative differences are less than 10% through the water column. Greater differences are observed for the Corona ADCP station (≈ 30%) and for the Chilen ADCP station (≈ 20%), which are located outside Chacao Channel boundaries, where no high-resolution bathymetry was available. From the measurements, ebb-averaged horizontal speeds are of higher magnitude, this trend is reproduced in the model results for all except at the Chocoi station, which is located in the west edge of the high-resolution bathymetry.

Model results are also analyzed in terms of the total turbulent kinetic energy (TKE) and TKE dissipation rates, which are given by a turbulence closure scheme in the model. These turbulence parameters are compared with estimates from the TTM measurements. This analysis is included since turbulence parameters are key inputs for tidal energy infrastructure design. Due to the timing difference between the model run and the TTM measurements, continuous tidal cycles from the model output have been selected to perform the comparisons, following the matching methodology described in Thyng et al. (2013) [39]. The alignment of numerical results and field data uses the best match between along-channel tidal currents at the depth bin closest to the TTM target height.

Turbulent kinetic energy and TKE dissipation rates are a direct output from the FVCOM numerical model. The TKE from the model, defined as $TKE = 1/2(\overline{u'^2} + \overline{v'^2} + \overline{w'^2})$, includes the three components of velocity fluctuations and is assumed to be isotropic [27,32]. The TKE from the field data is obtained from the autocorrelation of the velocity fluctuations using 5 min

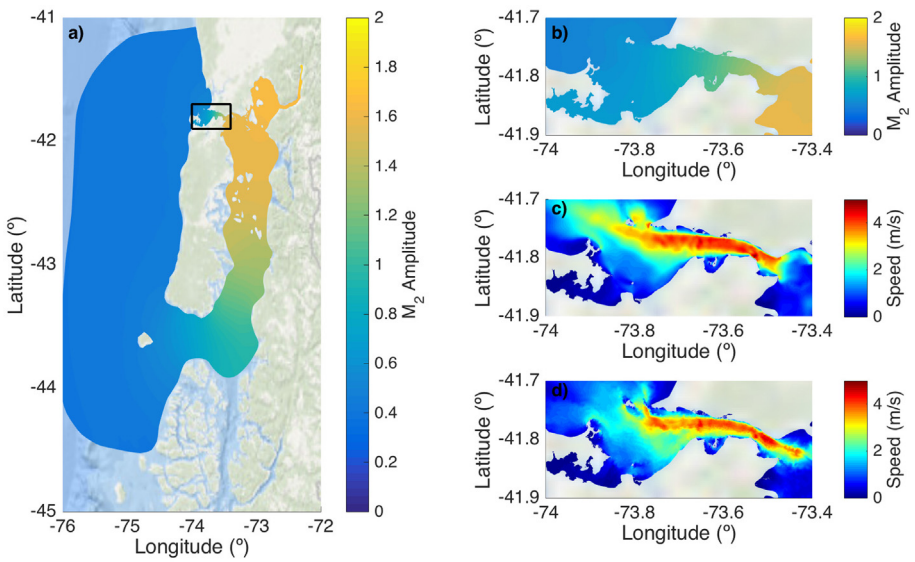

Fig. 10. FVCOM results: a) M_2 Tidal elevation component along the CIS, black rectangle denotes zoom-in area within Chacao Channel, b) M_2 Tidal elevation component within Chacao Channel, c) maximum ebb depth averaged velocities, and d) maximum flood depth averaged velocities.

burst as used in the TKE spectra calculations. The field TKE dissipation rate is estimated from the isotropic portion of the TKE spectra as explained in Section 4.2.

Time series of observed horizontal speed, total TKE, and TKE dissipation rates, together with numerical results from the selected period, are shown in Fig. 11. There is good agreement for the tidal current horizontal speed and in the TKE dissipation rates, however the total TKE from measurements greatly exceeds the total TKE estimate from FVCOM. As noted in [39], this difference likely is due to the isotropic turbulent kinetic energy assumption and the scales represented in the turbulence closure model [32]. The Chacao Channel measurements indicate the dominance of anisotropic turbulence at low frequencies, yet this portion of the TKE is not captured by the model. To obtain a fair comparison between measured and modeled total TKE, a new estimate using only the isotropic portion of the field data spectra has been calculated. This isotropic-only TKE is estimated as $TKE_{iso} \approx 3/2\overline{u_{iso}'^2}$ and is obtained from the numerical integration of the isotropic portion of the u' TKE spectra (between 0.2 and 2 Hz). Note that this isotropic TKE corresponds to what is called Classic TKE in [39]. The FVCOM TKE output agrees well with the isotropic TKE estimate from field measurements, indicating that the model does well reproducing specific turbulence parameters, but that the results must be used cautiously if large scales of turbulence are of interest. A technique developed in [39] can be applied to extrapolate model results in order to account for missing low-frequency TKE.

3.4. Kinetic power density

Estimation of the kinetic power density available in Chacao Channel is presented below using both ADCP measurements and FVCOM results. Power density, P, is estimated as:

$$P = \frac{1}{2}\rho U^3 \tag{3}$$

where ρ is the water density and U is the horizontal speed. Vertical profiles of time-averaged power density from ADCP data and from FVCOM results are calculated using the methods from [5] at each ADCP station, which uses the horizontal velocity magnitude in the calculation of power density [5]. These profiles are shown in Fig. 12. Power density is higher at the stations within the narrow area of Chacao Channel. It is approximately 2 kWm^{-2} at hub-height (10 m above sea-bottom), increasing up to 4 kWm^{-2} about 30 m from the sea-bottom. For comparison, the values at the Admiralty Inlet prospective tidal energy site in Puget Sound, WA, USA, are about 2 kWm^{-2} at 30 m above the sea-bottom. Overall, the power density exceeds 5 kW/m^{-2} approximately 20% of the time at mid depth for the ADCP stations located within Chacao Channel (i.e except at Corona and Chilen stations). Differences between power estimations from ADCP data and those from FVCOM results are explained by the difference in horizontal velocities between measurements and model. The differences are amplified in the power profiles (in comparison with the velocity profiles) since power proportional to the cube of velocity.

Fig. 13 panels a) and b) show maps of time-averaged and maximum power density estimated using depth-averaged horizontal velocities from the FVCOM model (time-averaged over the modeled period). The area with the highest average and

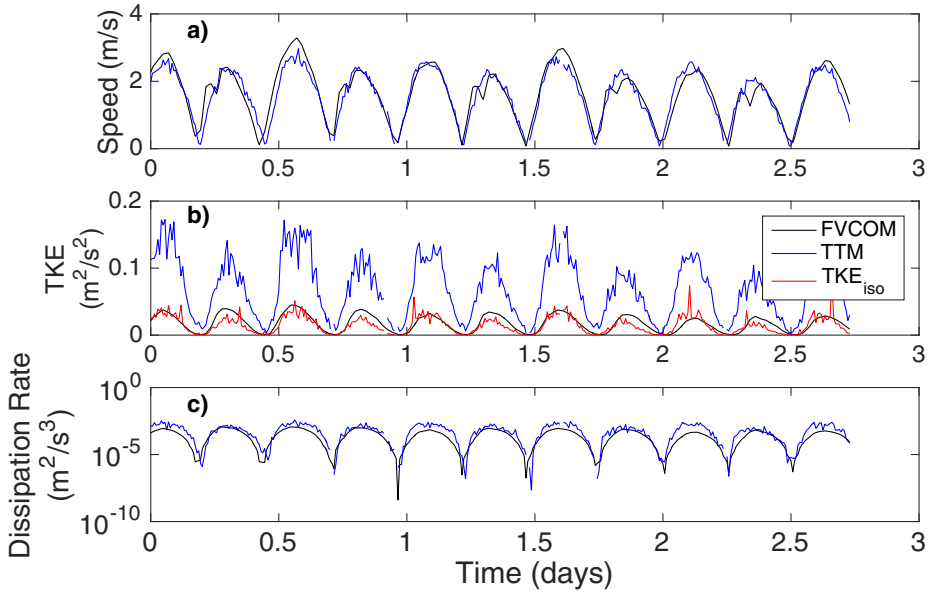

Fig. 11. Turbulence parameters at Young Station for selected FVCOM tidal cycles and comparable field data results: a) Horizontal speed, b) Turbulent Kinetic Energy (TKE), and c) TKE Dissipation Rate. Black lines correspond to FVCOM results, blue lines correspond to data from TTM ADVs, and red line correspond to the isotropic TKE estimated from the TKE spectra.

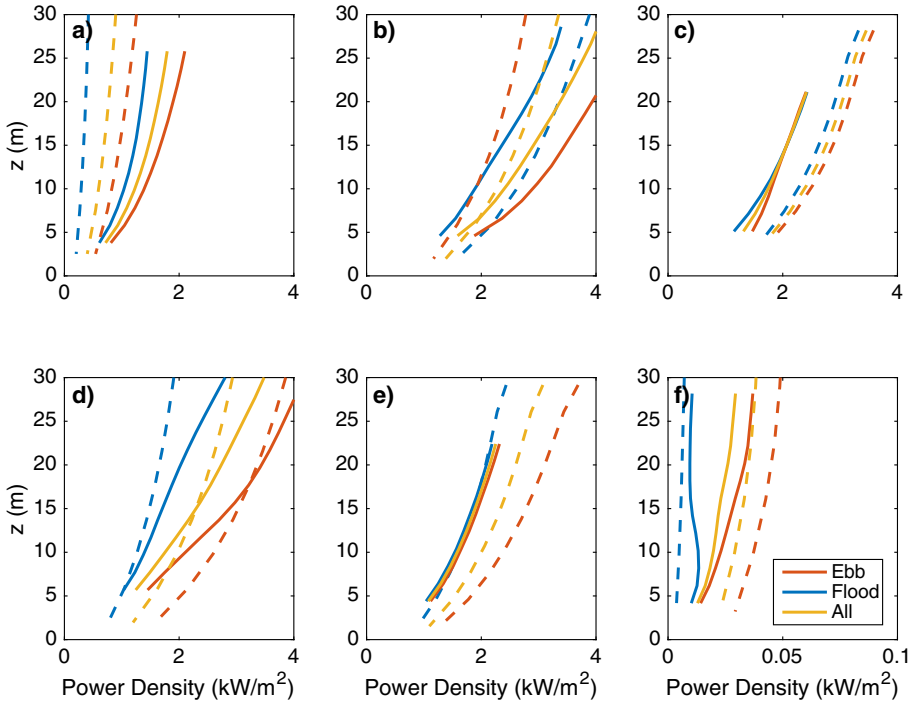

Fig. 12. Vertical profiles of time-averaged power density estimates at ADCP stations: a) Corona, b) Chocoi, c) Amazonas, d) Young, e) Caulin, and f) Chilen. Ebb tide is in red, flood tide is in blue, and all records are in yellow. Dashed lines correspond to power estimates using FVCOM velocity profiles. Note the different scale in the Chilen station plot, this ADCP was located outside of the main Chacao Channel area.

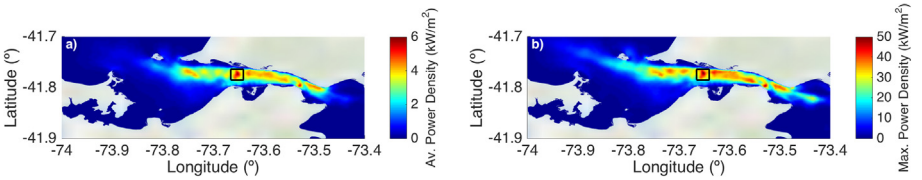

Fig. 13. Power density estimates from FVCOM results, using depth averaged velocities in kWm^{-2}: a) Average power density, and b) Maximum power density. Black rectangle delimits the area with the higher averaged power density.

maximum power density is located at (41.78 S, 73.65 W, marked with a square in Fig. 13). This area is close to the Caulin ADCP station, which shows the less ebb/flood asymmetry in horizontal velocities, hence in power density. Depth at this area is about 60 m and currents exceed 1.5 ms^{-1} approximately 60% of the time.

3.4.1. Power generation

A simple horizontal-axis turbine model is used to estimate power generation at the ADCP stations within Chacao Channel (Chilen ADCP station is excluded due to its low power density). The turbine power output is estimated using the methodology from [5], which estimates the power output as a function of horizontal speed, the angle between the current and the turbine rotor, the turbine swept area, the overall turbine efficiency, and the water density. For this study, turbine parameters from a twin-rotor SeaGen turbine available in [4] are used in the generation analysis. Each rotor in the model is 16 m in diameter. The cut-in speed and rated speed are 1 ms^{-1} and 2.68 ms^{-1}, respectively [4]. The overall efficiency, assumed to be constant during all operating conditions, is 30% [4]. These parameters result in 0.6 MW rated power rotors. Hub-height is set at 15 m above the sea-bottom.

Power generation estimates based on ADCP velocity measurements are shown in Table 2. At all tested sites, a single turbine would operate at least $\sim$ 70% of the time, with average annual energy production above 1500 MWh. For example, a single turbine located at the Chocoi site would operate 99% of the time, generating an average of 0.33 MW. The capacity factor, defined as the ratio of average generated power and turbine rated power, is estimated to be 28%, which results in an average annual energy production (AEP) of $\sim$ 2800 MWh. The same turbine located at the Young site, would operate 70% of the time, generating an average of 0.3 MW, with a capacity factor of 26%, resulting in an AEP of $\sim$ 2600 MWh.

Table 2
Power generation estimates for a twin-rotor SeaGen horizontal-axis turbine. Power is estimated using ADCP velocity measurements.

Location	Av. Power (MW)	Max. Power (MW)	C.F. (%)	Op. time (%)	A.E.P (MWh)
Corona	0.18	1.19	0.15	0.99	1,585
Chocoi	0.33	1.19	0.28	0.99	2,880
Amazonas	0.27	1.19	0.23	0.69	2,386
Young	0.30	1.19	0.26	0.70	2,665
Caulin	0.26	1.19	0.22	0.69	2,250

4. Discussion

4.1. Ebb/flood asymmetry

The Ebb/Flood asymmetry is defined as the ratio of the ebb and the flood time-averaged horizontal velocities [5]. An ebb/flood asymmetry in the tidal currents is observed in both the measured tidal currents and in the model results at Chacao Channel.

Figs. 10 c) and d) show maximum ebb and flood depth averaged velocities from the FVCOM model. Towards the west end of the channel (close to Carelmapu and Ancud villages), maximum depth-averaged velocities are higher during ebb than during flood, which is consistent with the findings from the ADCP measurements.

From the ADCP stations, it is found that the ebb/flood asymmetry is more significant at the Corona, Chocoi and Young ADCP stations, where it is observed to be above 50% at 15 m from the sea-bottom. At the Amazonas ADCP station, the asymmetry is higher below 10 m from the sea-bottom (20%), and at the Caulin station, ebb/flood asymmetry is less than 1%.

The ebb dominance might be explained by residual flows oriented seaward. According to [20], residual flows vary in magnitude and direction across Chacao Channel due to nonlinear interactions between the currents and the channel's bathymetry [20]. In other regions, residual flows are often an estuarine exchange driven by river discharge into an inland sea. Chacao Channel residual flows, calculated by applying a 40-h filter to the ADCPs stations data set [5]. Residual flows at the Young ADCP station are shown in Fig. 14. Residual flows are predominantly seawards during most of the deployment at Corona, Chocoi and Young stations, with residual flows reaching 0.2 ms^{-1} during spring tide. At Amazonas the residual flow is less than 0.1 ms^{-1}, and at Caulin it varies evenly from seaward to landward during the deployment period. Residual flows are enhanced in magnitude during spring tides, but the measurement duration is too short to observe a seasonal component in the residual flow. From the data, it is not possible to identify the source of the residual flows. However, a principal component analysis (PCA) [40] of the measured currents at the Young ADCP station shows that approximately 99.8% of their variability is explained by barotropic circulation (first PCA mode), while only a 0.14% of the variability is explained by baroclinic circulation (second PCA mode), the following modes account for less than 0.1% of the variability in the currents.

4.2. TKE balance

In order to characterize the dynamics of turbulence at the Young site in Chacao Channel, and to understand where turbulence is being produced and dissipated, the full TKE balance is examined, which can be written as:

$$\frac{D}{Dt}(TKE) = \nabla T + \mathscr{P} - \varepsilon \tag{4}$$

Where D/Dt is the rate of change of TKE, T is the turbulent transport of TKE, $\mathscr{P}$ is the production of TKE from the mean flow shear (positive production) and from buoyancy (negative production), and ε represents the dissipation of TKE to heat and sound.

The dissipation rate of TKE, ε, is related to the isotropic portion of the TKE frequency spectrum by:

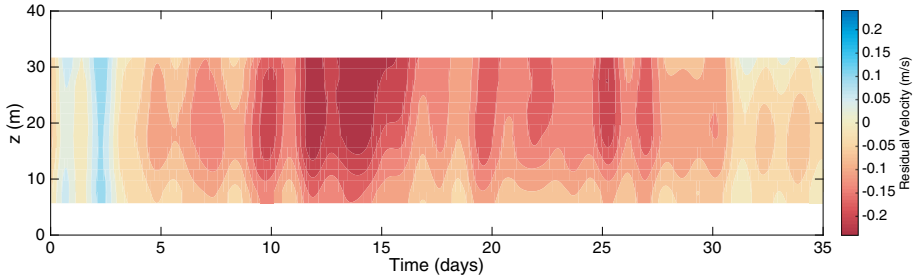

Fig. 14. Residual flow at Young station calculated by applying a 40-h filter to the ADCP data. Analysis performed with methodology from [5].

$$S(f) = \alpha \varepsilon^{2/3} f^{-5/3} \left(\frac{\bar{u}}{2\pi} \right)^{2/3} \tag{5}$$

where α is a constant equal to 0.69 when using the vertical TKE spectra, ε is the dissipation rate, f is the frequency and $\overline{u}$ is the mean along-channel velocity. The dissipation of TKE is calculated from the 5-min vertical TKE spectra presented in Section 3.2. Each 5-min spectra was multiplied by $f^{-5/3}$ in order to get a compensated spectra, which is expected to be horizontal (flat) in the inertial subrange. Different ranges of frequencies, between 0.2 and 2 Hz, were considered in the fitting of the compensated spectra to a linear model. The linear fit with the minimum slope (closest to zero) was chosen for the dissipation rate calculation, using at least 51 frequency bands (each of 0.01 Hz). The minimum slopes of the best linear fit to the compensated spectra varied between ±0.003. The mean of the best linearly fitted compensated spectra was estimated, and ϵ was calculated by solving $\overline{S_{comp}} = \alpha \varepsilon^{2/3} \left(\frac{\bar{u}}{2\pi} \right)^{2/3}$.

In a well-mixed environment such as Chacao Channel [20], TKE loss (negative production) due to buoyancy is expected to be negligible and TKE is primarily produced by the mean flow shear. If TKE is mainly produced by bottom stress driving vertical shear, and thus lateral shear is negligible, then TKE production can be approximated as:

$$\mathscr{P} \approx -\overline{u'w'} \frac{\delta \overline{u}}{\delta z} \tag{6}$$

which requires an estimation of the $\overline{u'w'}$ Reynolds stress and the mean flow vertical shear $\delta\overline{u}/\delta z$. The TTM measurements provide turbulence measurements at a single location in the water column, thus it is not possible to estimate the mean flow vertical shear directly from the those velocity measurements. Instead, the tidal current vertical profiles from the multi-month ADCP measurements of velocity at the Young station are used. The law of the wall assumption is used in order to estimate the approximate TKE production from the ADCP measurements as follows. Considering a constant stress layer, the $\overline{u'w'}$ Reynolds stress is linked to the bottom stress, and to the shear velocity u_* through the drag law as

$$\tau_b = -\rho \overline{u'w'} = \rho u_*^2. \tag{7}$$

For a fully developed turbulent flow, the law of the wall provides the following definition for the mean flow vertical shear,

$$\frac{\delta \overline{u}}{\delta z} = \frac{u_*}{\kappa z} \tag{8}$$

were u_* is the shear velocity, κ is de Von Kármán constant, equal to 0.41, and z de distance from the wall, or bottom, where the gradient is defined. Combining Eqs. (7) and (8), the TKE production P can be estimated as

$$\mathscr{P} = \frac{u_*^3}{\kappa z}. \tag{9}$$

The shear velocity u_* is estimated by fitting a logarithmic profile to the horizontal velocity profile obtained from integration of Eq. (8), to each of the 10 min averaged vertical profiles at Young station, following the methodology described in [41].

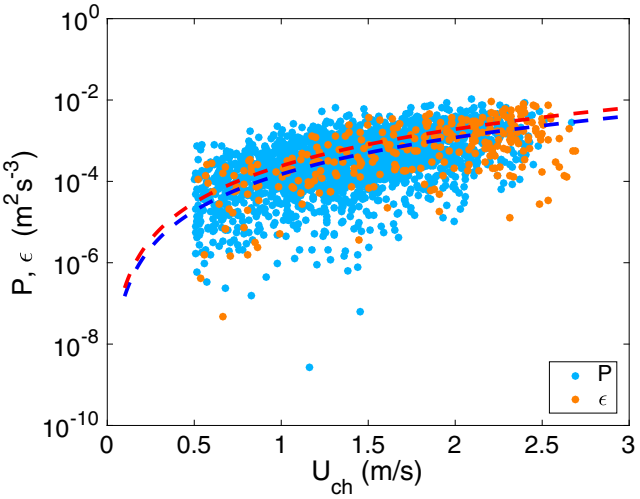

Fig. 15. Approximate TKE Production and Dissipation rates estimates for different along-channel mean flow conditions at the Young site. Light blue and orange dots respectively represent TKE production and dissipation rates. Blue and red dashed lines represent the best non-linear fit to $\sim u^3$ for P and ε estimates respectively.

Independent TKE production estimates and dissipation estimates are compared in Fig. 15 for the Young site. As seen in Fig. 15, the dissipation rate strongly follows Kolmogorov's self similarity theory $\varepsilon \sim \frac{u^3}{L}$ [37], were L is typically a length scale given by the depth (in the absence of stratification). Although the production estimate is noisier than the dissipation estimate, a fairly good agreement between TKE the production and TKE dissipation is observed at the targeted depth. This suggests that the turbulence observed at the Young site is locally produced by bottom stress, as opposed to being produced elsewhere and advected to the site.

5. Conclusions

The tidal energy resource of Chacao Channel is characterized from field measurements and assessed from numerical simulations. Six sites along Chacao Channel are characterized using bottom-mounted ADCP measurements. Local variability of currents and turbulence are characterized at the Young site (offshore Carelmapu) using shipboard ADCP measurements and a mid-water mooring.

The results show that several areas of Chacao Channel are suitable for tidal current energy extraction, with mean kinetic power density above 5 kWm^{-2} more than 20% of the time at depths less than 60 m. This large kinetic resource is associated with sea elevation tidal harmonic components within Chacao Channel that increase in amplitude from west to east and significantly change in phase (1.2m and 20° respectively for M_2). The underlying dynamic is tidal wave resonance within the northern portion of the Chilean Inland Sea [21].

Tidal currents are largely harmonic along the channel, with currents that surpass 4 ms^{-1} during spring tides in the narrower parts of the channel. Currents above 1ms^{-1} are observed more than 65% of the time during a monthly tidal cycle. Despite the ubiquitous high currents, significant local variability is observed in the vicinity of the Young site, with currents increasing in about 1 ms^{-1} within 500 m offshore of Carelmapu. These variations show the necessity to conduct higher resolution measurements and modeling when defining crucial aspects of tidal energy projects, such as turbine array location and distribution (sometimes referred to as micro-siting).

Turbulent velocity fluctuations are analyzed at the Young site using the compliant mooring approach from [26]. Turbulence intensities range between 5 to 20% and do not show a clear relation with the mean flow. Spectral analysis shows highly energetic anisotropic turbulence, probably related to the bathymetric features of the channel, together with a clear isotropic energy cascade that follows the theoretical relation of $f^{-5/3}$. Dissipation rate estimates from the TKE spectra follow the theoretical relation with $\bar{u}^3$. The turbulent kinetic energy budget suggest a local TKE production-dissipation balance at mid depth, implying that turbulence is locally produced and dissipated, and that TKE transport is less significant.

The FVCOM hydrodynamic model correctly captures the tidal dynamics within the Chilean Internal Sea and Chacao Channel; surface elevation and tidal ellipses agree well with measurements. In terms of turbulence parameters, the model correctly reproduces the isotropic portion of the turbulent kinetic energy. However, the model fails in describing the anisotropic portion of the turbulent kinetic energy, because these scales are outside of the formulation of the turbulence closure scheme. Thus, numerical model results are valuable for tidal resource energy application, but must be used with caution for tidal turbine design inputs (i.e., turbulence) [39]. This constraint can be overcome by following the method developed in [39] to extrapolate the scales not captured by the model.

The gathered information and numerical model results constitute a knowledge base for future tidal energy development in the region, including more detailed resource assessments and definition of priority sites. Model results can also be used for integration with high resolution turbulence models of tidal energy turbines. Other areas of application include contaminant dispersion, sediment transport, and analysis of residual flows.

Acknowledgements

The Instituto Nacional de Hidráulica provided the tidal elevation measurements. Bentos S.A. collected the fixed ADCP measurements, under a sub-contract with PUC. The authors collected the shipboard ADCP and moored ADV measurements, with help from Joe Talbert, Alex de Klerk and Christopher Basset, along with Capt. Eduardo Hernández and the crew of R/V Dr. Jurgen Winter. This work has been supported by Conicyt - Fondef Project D09i1052, the Office of Naval Research-Global and HydroChile S.A. Maricarmen Guerra thanks the support of the Fulbright and the Conicyt - Becas Chile doctorate fellowship programs. Rodrigo Cienfuegos and Leandro Suarez thank the support of MERIC – Marine Energy Research & Innovation Center (14CEI2-28228).

References

[1] Ministerio de Energía de Chile, Energy 2050 - Chile Energy Policy, Tech. rep., Ministerio de Energía de Chile, 2015.
[2] R. Raineri, Chile: where it all started, Electricity Market Reform: An International Perspective, 2006, 77–108.
[3] J. Cruz, M. Thomson, E. Stavroulia, R. Rawlinson-Smith, Preliminary site selection-chilean marine energy resources. report for the inter-american development bank, Tech. rep., Garrad Hassan and Partners, 2009.
[4] M. Lewis, S. Neill, P. Robins, M. Hashemi, Resource assessment for future generations of tidal-stream energy arrays, Energy 83 (2015) 403–415.
[5] B. Polagye, J. Thomson, Tidal energy resource characterization: methodolgy and field study in Admiralty Inlet, Puget Sound, USA, Proc. IMechE, Part A: J. Power Energy 227 (3) (2013) 352–367, https://doi.org/10.1177/0957650912470081.

[6] C. Legrand, Assessment of tidal energy resource: Marine renewable energy guides, European Marine Energy Centre, 2009.
[7] J. Goundar, R. Ahmed, Marine current energy resource assessment and design of a marine current turbine for fiji, Renewable Energy 65 (2014) 14–22.
[8] N. Carpman, K. Thomas, Tidal resource characterization in the folda fjord, norway, Int. J. Mar. Energy 13 (2016) 27–44.
[9] M. Thiébaut, A. Sentchev, Tidal stream resource assessment in the dover strait (eastern english channel), Int. J. Mar. Energy 16 (2016) 262–278.
[10] M. Palodichuk, B. Polagye, J. Thomson, Resource mapping at tidal energy sites, J. Ocean. Eng. 38 (3) (2013) 433–446, https://doi.org/10.1109/JOE.2012.2227578.
[11] Z. Yang, T. Wang, A. Copping, Modeling tidal stream energy extraction and its effects on transport processes in a tidal channel and bay system using a three-dimensional coastal ocean model, Renewable Energy 50 (2013) 605–613, https://doi.org/10.1016/j.renene.2012.07.024, http://www.sciencedirect.com/science/article/pii/S0960148112004508.
[12] H. Tang, S. Kraatz, K. Qu, G. Chen, N. Aboobaker, C. Jiang, High-resolution survey of tidal energy towards power generation and influence of sea-level-rise: a case study at coast of new jersey, USA, Renew. Sustain. Energy Rev. 32 (2014) 960–982, https://doi.org/10.1016/j.rser.2013.12.041, http://www.sciencedirect.com/science/article/pii/S1364032113008551.
[13] C. Garrett, P. Cummins, Limits to tidal current power, Renewable Energy 33 (11) (2008) 2485–2490.
[14] J. Thomson, B. Polagye, V. Durgesh, M. Richmond, Measurements of turbulence at two tidal energy sites in Puget Sound, WA, J. Ocean. Eng. 37 (3) (2012) 363–374.
[15] L. Chamorro, C. Hill, S. Morton, C. Ellis, R. Arndt, F. Sotiropoulos, On the interaction between a turbulent open channel flow and an axial-flow turbine, J. Fluid Mech. 716 (2013) 658–670.
[16] T. Blackmore, L. Myers, A. Bahaj, Effects of turbulence on tidal turbines: Implications to performance, blade loads, and condition monitoring, Int. J. Mar. Energy 14 (2016) 1–26.
[17] P. Pyakurel, J. VanZwieten, M. Dhanak, N. Xiros, Numerical modeling of turbulence and its effect on ocean current turbines, Int. J. Mar. Energy 17 (2017) 84–97, https://doi.org/10.1016/j.ijome.2017.01.001, www.sciencedirect.com/science/article/pii/S2214166917300012.
[18] T. Blackmore, W. Batten, A. Bahaj, Influence of turbulence on the wake of a marine current turbine simulator, in: Proceedings of the Royal Society of London A: Mathematical, Physical and Engineering Sciences, Vol. 470, The Royal Society, 2014, pp. 20140331.
[19] E. Osalusi, J. Side, R. Harris, Structure of turbulent flow in emec's tidal energy test site, Int. Commun. Heat Mass Transfer 36 (5) (2009) 422–431.
[20] M. Cáceres, A. Valle-Levinson, L. Atkinson, Observations of cross-channel structure of flow in an energetic tidal channel, J. Geophys. Res.: Oceans (1978–2012) 108 (C4).
[21] C. Aiken, Barotropic tides of the chilean inland sea and their sensitivity to basin geometry, J. Geophys. Res.: Oceans (1978–2012) 113 (C8).
[22] S. Pantoja, J. Iriarte, G. Daneri, Oceanography of the chilean patagonia, Cont. Shelf Res. 31 (3) (2011) 149–153.
[23] R. Hucke-Gaete, L. Osman, C. Moreno, K. Findlay, D. Ljungblad, Discovery of a blue whale feeding and nursing ground in southern chile, Proc. R. Soc. London B: Biol. Sci. 271 (Suppl 4) (2004) S170–S173.
[24] B. Vernazzani, C. Carlson, E. Cabrera, R. Brownell Jr., Chilean blue whales off isla grande de Chiloe, 2004–2010: distribution, site-fidelity and behaviour, J. Cetacean Res Manage 12 (3) (2012) 353–360.
[25] J. Castilla, P. Manŕquez, E. Fica, V. Ortiz, Proyecto fondef d09i1052: Uso del espacio marítimo: situaciń pesquero-acuícola en la zona de estudio en el canal de chacao, Unpublished (2012) 1–75.
[26] J. Thomson, L. Kilcher, M. Richmond, J. Talbert, A. deKlerk, B. Polagye, M. Guerra, R. Cienfuegos, Tidal turbulence spectra from a compliant mooring, in: Proc. of the 1st Marine Energy Technical Symposium (METS), Washington D.C., 2013.
[27] C. Chen, H. Liu, R. Beardsley, An unstructured, finite-volume, three-dimensional, primitive equation ocean model: application to coastal ocean and estuaries, J. Atmos. Oceanic Technol. 20 (2003) 159–186.
[28] S. Harding, L. Kilcher, J. Thomson, Turbulence measurements from compliant moorings – Part I: motion characterization, J. Atmos. Oceanic Technol.
[29] L. Kilcher, S. Harding, J. Thomson, S. Nylund, Turbulence measurements from compliant moorings – Part II: motion correction, J. Atmos. Oceanic Technol.
[30] C. Chen, R. Beardsley, G. Cowles, J. Qi, Z. Lai., G. Gao, D. Stuebe, Q. Xu, P. Xue, J. Ge, et al., An Unstructured-grid, Finite-volume Community Ocean Model: FVCOM User Manual, third ed., SMAST/UMASSD Tech., 2013.
[31] G. Egbert, S. Erofeeva, Efficient inverse modeling of barotropic ocean tides, J. Atmos. Oceanic Technol. 19 (2) (2002) 183–204.
[32] G. Mellor, T. Yamada, Development of a turbulence closure model for geophysical fluid problems, Rev. Geophys. Space Phys. 20 (4) (1982) 851–875.
[33] J. Smagorinsky, General circulation experiments with the primitive equations: I. The basic experiment, Mon. Weather Rev. 91 (3) (1963) 99–164.
[34] R. Pawlowicz, B. Beardsley, S. Lentz, Classical tidal harmonic analysis including error estimates in matlab using ttide, Comput. Geosci. 28 (8) (2002) 929–937.
[35] D. Goring, V. Nikora, Despiking acoustic doppler velocimeter data, J. Hydraulic Eng. 128 (1) (2002) 117–126.
[36] K. McCaffrey, B. Fox-Kemper, P. Hamlington, J. Thomson, Characterization of turbulence anisotropy, coherence, and intermittency at a prospective tidal energy site: observational data analysis, Renewable Energy 76 (2015) 441–453.
[37] A. Kolmogorov, Dissipation of energy in the locally isotropic turbulence, Dokl. Akad. Nauk SSR 30 (1941) 301–305.
[38] B. Brumley, R. Cabrera, K. Deines, E. Terray, Performance of a broad-band acoustics Doppler current profiler, J. Ocean. Eng. 16 (4).
[39] K. Thyng, J. Riley, J. Thomson, Inference of turbulence parameters from a roms simulation using the k-ε closure scheme, Ocean Model. 72 (2013) 104–118.
[40] C. Edwards, H. Seim, Complex eof analysis as a method to separate barotropic and baroclinic velocity structure in shallow water, J. Atmos. Oceanic Technol. 25 (5) (2008) 808–821.
[41] C. Bassett, J. Thomson, B. Polagye, Sediment generated noise and bed stress in a tidal channel, J. Geophys. Res.: Oceans 118 (2013) 1–17, https://doi.org/10.1002/jgrc.20169.